A novel photonic crystal fiber refractive index sensor with ultra wide detection range based on surface plasmon resonance effect

Yuwei Qu[a)] Jinhui Yuan[a)b)*] Shi Qiu[a)] Xian Zhou[b)] Binbin Yan[a)]

Qiang Wu[d)e)*] Bin Liu[e)] Kuiru Wang[a)] Xinzhu Sang[a)] Keping Long[b)] Chongxiu Yu[a)]

a State Key Laboratory of Information Photonics and Optical Communications, Beijing University of Posts and Telecommunications, Beijing 100876, China

b Research Center for Convergence Networks and Ubiquitous Services, University of Science & Technology Beijing (USTB), Beijing 100083, China

c Department of Physics and Electrical Engineering, Northumbria University, Newcastle upon Tyne, NE1 8ST, United Kingdom

d Key Laboratory of Nondestructive Test (Ministry of Education), Nanchang Hangkong University, Nanchang 330063, China

**yuanjinhui81@bupt.edu.cn; qiang.wu@northumbria.ac.uk*

ABSTRACT In this paper, a novel photonic crystal fiber (PCF) refractive index (RI) sensor based on surface plasmon resonance (SPR) effect is proposed. With the full vector finite element method, the SPR-PCF RI sensor is designed, and the mode coupling effects between the X-polarization (X-pol) and Y-polarization (Y-pol) core modes and second-order surface plasmon polariton modes are analyzed. The simulation results show that the structure parameters of the proposed PCF have significant influences on the resonance wavelength drift and wavelength sensitivity (*WS*). Finally, in the RI range of 1.32 ~ 1.48, the average *WSs* of the X-pol and Y-pol core modes can reach -4735.83 nm/RIU and -4525.83 nm/RIU, respectively. Moreover, the maximum resolution (*R*) and figure of merits (*FOM*) of the X-pol and Y-pol core modes are 4.71×10^{-6} and 4.65×10^{-6} RIU, and 134 and 177 RIU^{-1}, respectively. Compared with other reported results, the proposed SPR-PCF RI sensor can achieve wide detection range, high average *WS*, good linearity, high *R*, and large *FOM*, so it will have important applications in the fields of biochemistry, medicine, and environmental science.

Keywords photonic crystal fiber; refractive index sensor; surface plasmon resonance; wavelength sensitivity; detection range

1. Introduction

In the late 1990s, the first photonic crystal fiber (PCF) was born, which opened a new chapter of optical fiber sensors [1-3]. Compared with the traditional optical fiber, the PCF has flexible and adjustable air holes in the cladding region [4-6]. With a variety of post-processing technologies the metal, liquid crystal, and other materials can be selectively filled into the air holes to achieve the sensing of different physical quantities [7-12].

Surface plasmon resonance (SPR) technology has developed rapidly in recent years. Based on this technology, many new devices have been developed, such as absorbers, sensors, polarization devices and so on [13-19]. Among them, the sensing technology based on SPR has been developed rapidly in the field of optical sensing [20-25]. The selective coating of the metal film or filling the metal nanowire in the air hole of the PCF could excite the SPR effect [26-27]. In recent years, the refractive index (RI) sensitivity of the liquid analytes using the SPR effect has been explored [28-33]. In 2019, Fan et al. reported a SPR-based PCF RI sensor coated with the nano-ring gold film. It was observed that an average wavelength sensitivity (*WS*) of 2150 nm/RIU in the RI range from 1.40 to 1.43 [34]. In 2020, Yasli et al. demonstrated a multi-channel PCF RI sensor based on the SPR effect comprised of silver and gold doped plasmonic layers. The maximum average *WSs* of the X-polarization (X-pol) and Y-polarization (Y-pol) core modes were 1892 and 2337 nm/RIU in the RI range from 1.33 to 1.366, respectively [35]. In 2020, Wang et al. proposed a SPR RI sensor based on a D-shaped Hi-Bi PCF, where the average *WS* of 3500 nm/RIU in the RI range from 1.33 to 1.34 and the figure of merit (*FOM*) of 39.8 RIU^{-1} were achieved [36]. In 2021, Wu et al. designed a gold film-coated D-shaped PCF RI sensor. For the analyte RI range of 1.345 to 1.375, the average *WS* of the sensor was up to 4494 nm/RIU [37].

In this paper, a novel PCF RI sensor based on the SPR effect is proposed. The mode coupling characteristics

between the X-pol and Y-pol core modes and second-order (2nd-order) surface plasmon polariton (SPP) mode are investigated by the full vector finite element method (FV-FEM). By analyzing the influences of the structure parameters on the resonance wavelength and *WS*, a SPR-PCF RI sensor with the average *WSs* of -4735.83 nm/RIU and -4525.83 nm/RIU for the X-pol and Y-pol core modes is obtained in the RI range of 1.32 to 1.48. Finally, the resolution (*R*) and *FOM* of the proposed SPR-PCF RI sensor are compared with other reported results.

2. Design of the SPR-PCF RI sensor

The cross-sectional structure of the proposed SPR-PCF RI sensor is shown in Fig. 1. The cross-sectional structure is arranged according to the regular hexagonal lattice. The diameter of the most central air hole is d_0, and the air hole is filled with liquid analyte with the RI n_a. The diameter of the left and right air holes adjacent to the air hole filled with the liquid analyte is d_1, and the diameter of the upper and lower four air holes is d_2. The upper part of the air hole filled liquid analyte has an air hole with a diameter of d_3 and it is coated with a gold nano film with a thickness of t. Compared with other metal materials, the gold material has stable chemical property, good biomolecular compatibility, and strong corrosion resistance. The other air holes are divided into the upper and lower parts and left and right parts, respectively. The diameters of the larger air holes in the upper and lower parts and the smaller air holes in the left and right parts are d_4 and d_5, respectively. The hole spacing between each two adjacent air holes is Λ. The backing material is the silica, whose material refractive index can be expressed by the Sellmeier equation [38]. In order to absorb the scattering loss, a perfect matching layer (PML) with the thickness Λ is designed on the outermost part of the proposed PCF and the refractive index of the PML is 0.03 higher than that of the silica material [39].

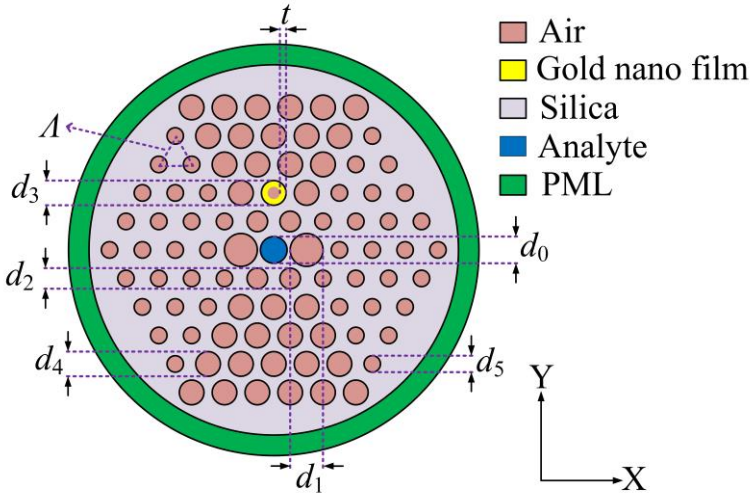

Fig. 1. The cross-sectional structure of the proposed PCF RI sensor.

The relative dielectric constant (ε_m) of the gold can be expressed by the Drude-Lorentz (D-L) model [40]

$$\varepsilon_m = \varepsilon_\infty - \frac{\omega_D^2}{\omega(\omega - j\gamma_D)} - \frac{\Delta\varepsilon \cdot \Omega_L^2}{(\omega^2 - \Omega_L^2) - j\Gamma_L\omega}, \quad (1)$$

where ω, ω_D, and γ_D are the angle frequency of the guided-wave, plasma frequency, and damping frequency,ε_∞ and $\Delta\varepsilon$ are the high frequency dielectric constant and the weighted coefficient, and Ω_L and Γ_L are the frequency and bandwidth of the Lorentz oscillator, respectively. The detailed parameter values of the D-L model are given in Table 1.

The FV-FEM can be used to simulate the effective refractive index (n_{eff}) of the mode field of the proposed PCF, and the confinement loss (L_C) of each mode of the proposed PCF can be described as following [41]

$$L_C = \frac{20}{\ln 10}\frac{2\pi}{\lambda}\mathrm{Im}[n_{\mathrm{eff}}]\times 10^6, \tag{2}$$

where λ is the wavelength of incident light incident, and Im[n_{eff}] is the imaginary parts of n_{eff} of each mode.

Table 1. The detailed parameter values of the D-L model for the gold nano film.

ε_∞	$\Delta\varepsilon$	$\omega_D/2\pi$ (THz)	$\gamma_D/2\pi$ (THz)	$\Omega_L/2\pi$ (THz)	$\Gamma_L/2\pi$ (THz)
5.9673	1.09	2113.6	15.92	650.07	104.86

The FV-FEM can be used to simulate the effective refractive index (n_{eff}) of the mode field of the proposed PCF, and the confinement loss (L_C) of each mode of the proposed PCF can be described as following [41]

$$L_C = \frac{20}{\ln 10}\frac{2\pi}{\lambda}\mathrm{Im}[n_{\mathrm{eff}}]\times 10^6, \tag{2}$$

where λ is the wavelength of incident light incident, and Im[n_{eff}] is the imaginary parts of n_{eff} of each mode.

The *WS* is an important parameter to determine the performance index of the sensor, which can be defined as [42]

$$WS = \frac{\Delta\lambda_{\mathrm{peak}}}{\Delta n_a}, \tag{3}$$

where $\Delta\lambda_{\mathrm{peak}}$ and Δn_a represent the change of the resonance wavelength at resonance peak and the change of the RI of the analyte measured, respectively.

In order to further prove the sensing characteristics of the sensor, the *R* and FOM are described as [43, 44]

$$R = \frac{\Delta n_a \cdot \Delta\lambda_{\mathrm{min}}}{\Delta\lambda_{\mathrm{peak}}}, \tag{6}$$

$$FOM = \frac{WS}{FWHM}, \tag{7}$$

where $\Delta\lambda_{\mathrm{min}}$ and *FWHM* indicate the wavelength resolution of the optical spectrum analyzer and the full-width at half-maximum of the resonance peak, respectively. At present, the wavelength resolution of the commonly used optical spectrum analyzer can reach 0.02 nm

3. Simulation Results and Discussion

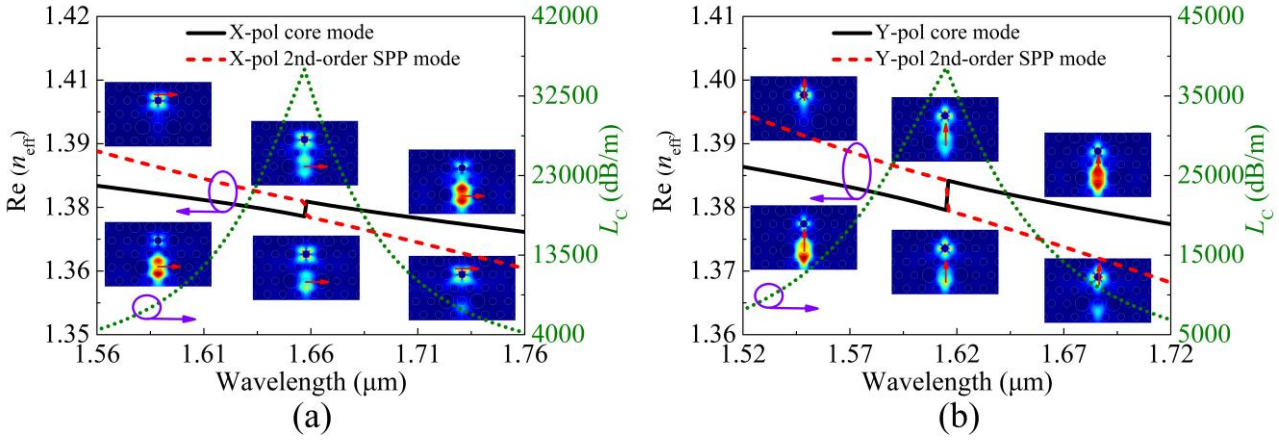

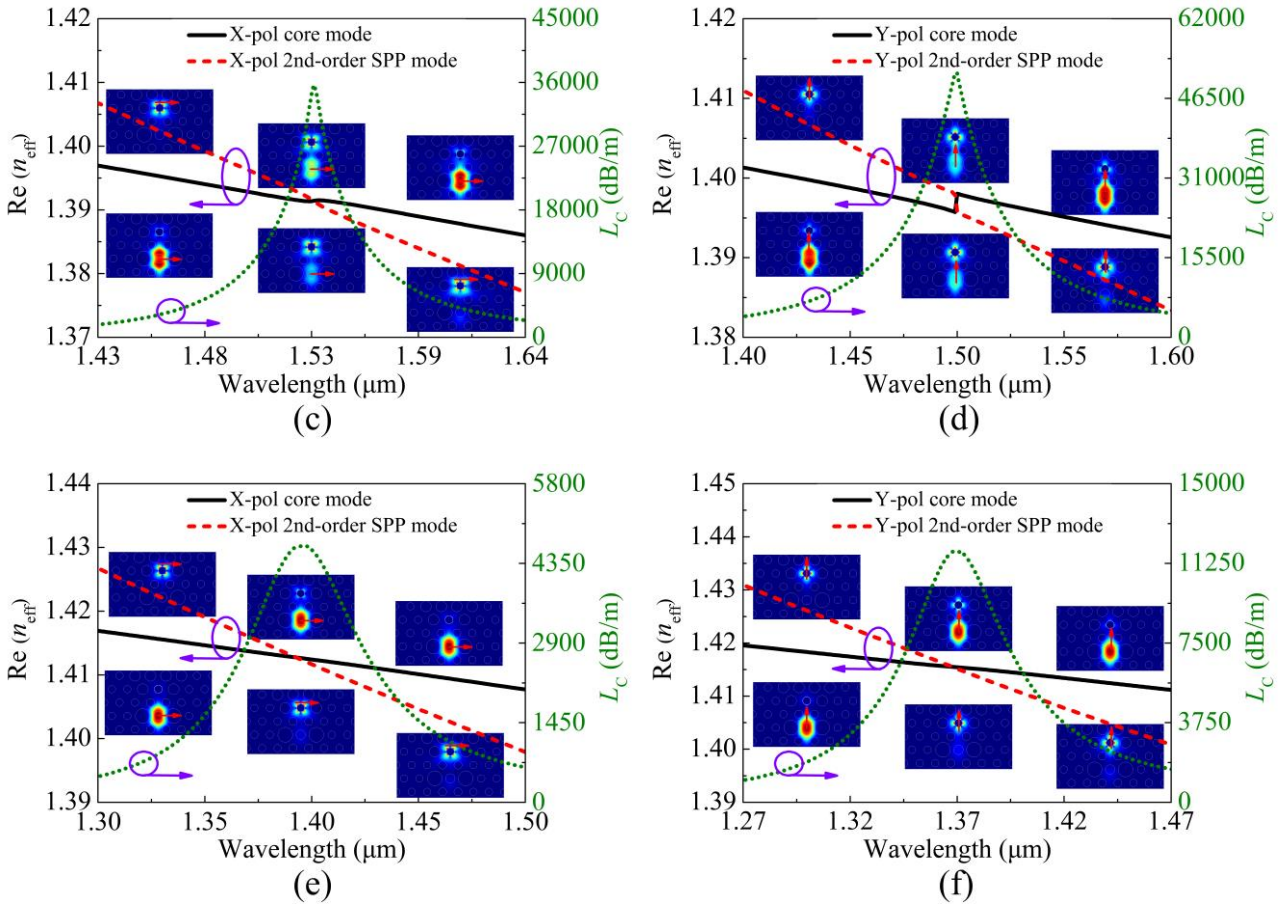

Fig. 2. The Re(n_{eff}) of the **(a)** X-pol and **(b)** Y-pol core mode and 2nd-order SPP mode, and the L_C of the X-pol and Y-pol core modes when n_a is 1.36. The Re(n_{eff}) of the **(c)** X-pol and **(d)** Y-pol core mode and 2nd-order SPP mode, and the L_C of the X-pol and Y-pol core modes when n_a is 1.40. The Re(n_{eff}) of the **(e)** X-pol and **(f)** Y-pol core mode and 2nd-order SPP mode, and the L_C of the X-pol and Y-pol core modes when n_a is 1.44. The illustrations in (a), (b), (c), (d), (e), and (f) show the mode field distributions of the X-pol and Y-pol core modes and 2nd-order SPP modes at different wavelengths.

In the simulation, the grid sequence type is physics-controlled mesh, and the grid element size is normal size. The complete grid contains 13928 domain elements and 1462 boundary elements, respectively. The initial structure parameters are set as following: d_0=1.4 μm, d_1=2.2 μm, d_2=1.2 μm, d_3=1.2 μm, d_4=1.6 μm, d_5=1.1 μm, Λ=2.3 μm, and t=50 nm. When n_a is chosen as 1.36, 1.40, and 1.44, respectively, the real parts of the effective refractive indices (Re(n_{eff})) of the X-pol and Y-pol core modes and the 2nd-order SPP modes and the L_C of the X-pol and Y-pol core modes are shown in Figs. 2(a) and 2(b), 2(c) and 2(d), and 2(e) and 2(f), respectively. From Figs. 2(a) and 2(b), at the shorter wavelength side, the Re(n_{eff}) of the X-pol and Y-pol core modes is smaller than that of the X-pol and Y-pol 2nd-order SPP modes, respectively, when n_a is 1.36. In contrast, at the longer wavelength side, the Re(n_{eff}) of the X-pol and Y-pol core modes is greater than that of the X-pol and Y-pol 2nd-order SPP modes, respectively. The Re(n_{eff}) of the X-pol and Y-pol core modes and 2nd-order SPP modes has an obvious mutation point at wavelengths 1.658 μm and 1.616 μm, respectively. According to the SPR effect and coupled mode theory [45-47], the X-pol and Y-pol core modes and 2nd-order SPP modes are completely coupled at wavelengths 1.658 μm and 1.616 μm, respectively, which are called as the resonance wavelengths. The L_C of the X-pol and Y-pol core modes generates the resonance peaks at resonance wavelengths 1.658 μm and 1.616 μm, respectively. It can also be seen from the illustrations in Figs. 2(a) and 2(b) that the mode field energy of the X-pol and Y-pol core modes and 2nd-order SPP modes has been strongly transferred at the resonance wavelengths 1.658

μm and 1.616 μm, while at the shorter and longer wavelength sides, most of the mode field energy of the X-pol and Y-pol core modes and 2nd-order SPP modes still remains unchanged. This phenomenon further shows that the X-pol and Y-pol core modes and 2nd-order SPP modes are completely coupled at resonance wavelengths 1.658 μm and 1.616 μm, respectively. From Figs. 2(c) and 2(d), the relationship between the Re(n_{eff}) of the X-pol and Y-pol core modes and 2nd-order SPP modes is consistent with that in Figs. 2(a) and 2(b), respectively, when n_a is 1.40. However, compared with Figs. 2(a) and 2(b), there is a less obvious mutation in the Re(n_{eff}) of the X-pol core mode and 2nd-order SPP mode at wavelength 1.536 μm, while there is still an obvious mutation at wavelength 1.5 μm. This indicates that the mode coupling strength of the X-pol core mode and 2nd-order SPP mode has not reached the complete coupling, but the Y-pol core mode and 2nd-order SPP mode are completely coupled at resonance wavelength. From the illustrations in Fig. 2(c), the mode field energy of the X-pol core mode and 2nd-order SPP mode has been weakly transferred at resonance wavelength 1.536 μm, while at the shorter and longer wavelength sides, most of the mode field energy of the X-pol core mode and 2nd-order SPP mode still remains unchanged. This phenomenon further indicates that the X-pol core mode and 2nd-order SPP mode are weakly coupled at resonance wavelength 1.536 μm. The L_C of the X-pol and Y-pol core modes also generates the resonance peaks at resonance wavelength 1.536 μm and 1.5 μm, respectively. From Figs. 2(e) and 2(f), at the shorter and longer wavelength sides, the relationship between the Re(n_{eff}) of the X-pol and Y-pol core modes and 2nd-order SPP modes is also consistent with that in Figs. 2(a) ~ 2(d), respectively, when n_a is 1.44. But there is no mutation in the Re(n_{eff}) of the X-pol and Y-pol core modes and 2nd-order SPP modes at wavelengths 1.393 μm and 1.368 μm, respectively. This indicates that the X-pol and Y-pol core modes and 2nd-order SPP modes are incompletely coupled at resonance wavelengths 1.393 μm and 1.368 μm, respectively. It is further confirmed from the illustrations in Figs. 2(e) and 2(f), that the mode field energy of the X-pol and Y-pol core modes and 2nd-order SPP modes still remains unchanged whether at the shorter wavelength, resonant wavelength, or longer wavelength. The L_C of the X-pol and Y-pol core modes also generates the resonance peaks at resonance wavelengths 1.393 μm and 1.368 μm, respectively.

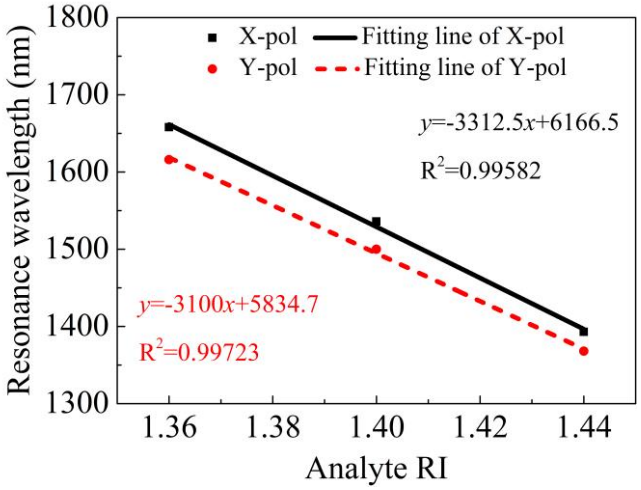

Fig. 3. The linear fitting results of the resonant wavelengths for the X-pol and Y-pol core modes with the analyte RI.

It can be concluded that when n_a increases from 1.36 to 1.44, the mode coupling between the X-pol and Y-pol core modes and 2nd-order SPP modes gradually changes from the complete coupling to the incomplete coupling, but the resonance peaks of the X-pol and Y-pol core modes always exist, and the corresponding resonance wavelengths gradually move toward the shorter wavelength. Therefore, the RI sensing can be realized by detecting the change of the resonance wavelength. Fig. 3 shows the linear fitting results of the resonant wavelengths for the X-pol and Y-pol core modes with the analyte RI. As seen from Fig. 3, the linear fitting results

of the X-pol and Y-pol core modes with the analyte RI are y= -3312.5x+6166.5 and y= -3100x+5834.7, respectively. And the coefficients of determination (R^2) are greater than 0.99 for both the X-pol and Y-pol core modes. In the RI range of 1.36 to 1.44, the average *WSs* of the X-pol and Y-pol core modes can achieve -3312.5 nm/RIU and -3100 nm/RIU, respectively. When the n_a is selected as 1.36, 1.40, and 1.44, respectively, in order to obtain the higher average *WSs*, it is necessary to analyze the variation of the L_C of the X-pol and Y-pol core modes with wavelength when the structural parameters of the proposed SPR-PCF are changed.

When n_a is selected as 1.36, 1.40, and 1.44, respectively, the variations of the L_C of the X-pol and Y-pol core modes with wavelength for different d_0 are shown in Fig. 4. From Figs. 4(a) and 4(b), when d_0 remains unchanged and n_a increases from 1.36 to 1.44, the resonance wavelengths of the X-pol and Y-pol core modes are blue-shifted, which is consistent with the previous results. Therefore, we only analyze the change of the resonance wavelengths of the X-pol and Y-pol core modes with d_0 when n_a is fixed at 1.36, 1.40, or 1.44. When n_a is fixed at 1.36 or 1.40, the resonance wavelengths of the X-pol and Y-pol core modes obviously occur to red-shift with the increase of d_0 from 1.2 to 1.6 μm. When n_a is fixed at 1.44, the resonance wavelengths of the X-pol and Y-pol core modes have a weak red-shift with the increase of d_0 from 1.2 to 1.6 μm. It is also found that the smaller n_a, the greater the red-shift amplitude of the X-pol and Y-pol core modes with the increase of d_0. This indicates that d_0 has a greater influence on the resonance wavelength shift when the complete coupling occurs. Hence, according to Eq. (3), the greater d_0, the greater the *WS*.

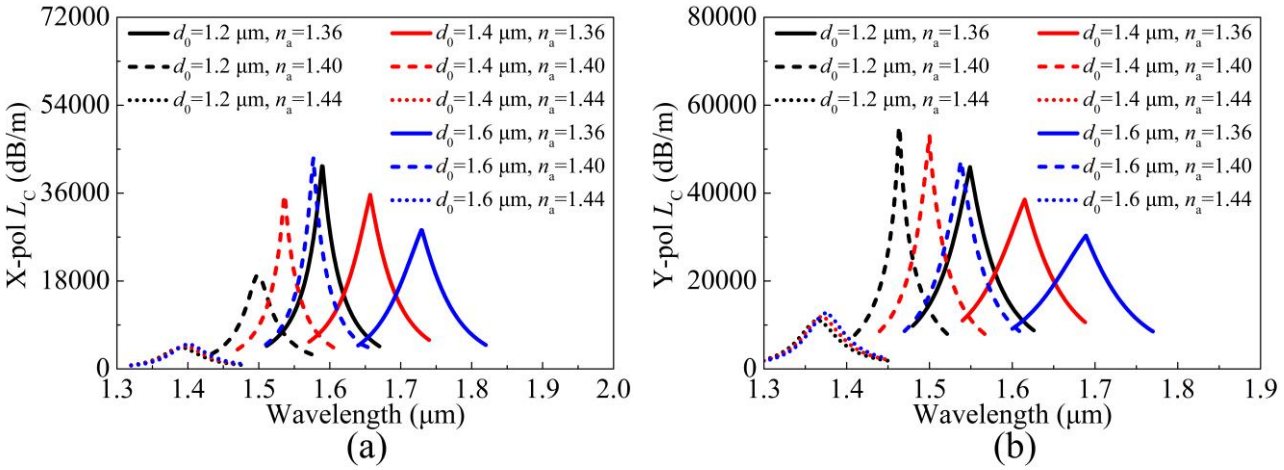

Fig. 4. The variation of the L_C of the **(a)** X-pol and **(b)** Y-pol core modes with wavelength for different d_0, when n_a is selected as 1.36, 1.40, and 1.44, respectively.

When n_a is selected as 1.36, 1.40, and 1.44, respectively, the variations of the L_C of the X-pol and Y-pol core modes with wavelength for different d_1 are shown in Fig. 5. From Figs. 5(a) and 5(b), when n_a is fixed at 1.36, 1.40, or 1.44, the resonance wavelengths of the X-pol and Y-pol core modes have a small red-shift with the increase of d_1 from 2.0 to 2.2 μm, and then have a larger red-shift as d_1 increases from 2.2 to 2.4 μm. However, when n_a is fixed at 1.36, the red-shift amplitude of the X-pol and Y-pol core modes with the increase of d_1 is the largest. This indicates that d_1 has a greater influence on the resonance wavelength when the complete coupling occurs. Hence, the greater d_1, the greater the *WS*.

When n_a is selected as 1.36, 1.40, and 1.44, respectively, the variations of the L_C of the X-pol and Y-pol core modes with wavelength for different d_2 are shown in Fig. 6. From Figs. 6(a) and 6(b), when n_a is fixed at 1.36 or 1.40, the resonance wavelengths of the X-pol and Y-pol core modes have a significant red-shift with the increase of d_2 from 1.1 to 1.3 μm. However, the resonance wavelengths of the X-pol and Y-pol core modes only have a

weak red-shift with the increase of d_2 from 1.1 to 1.3 μm when n_a is fixed at 1.44. In other words, as n_a increases from 1.36 to 1.44, the red-shift amplitude of the X-pol and Y-pol core modes decreases gradually with the increase of d_2. This also means that d_2 has a greater influence on the resonance wavelength when the complete coupling occurs. Therefore, a similar conclusion that the greater d_2, the greater the *WS* can be obtained.

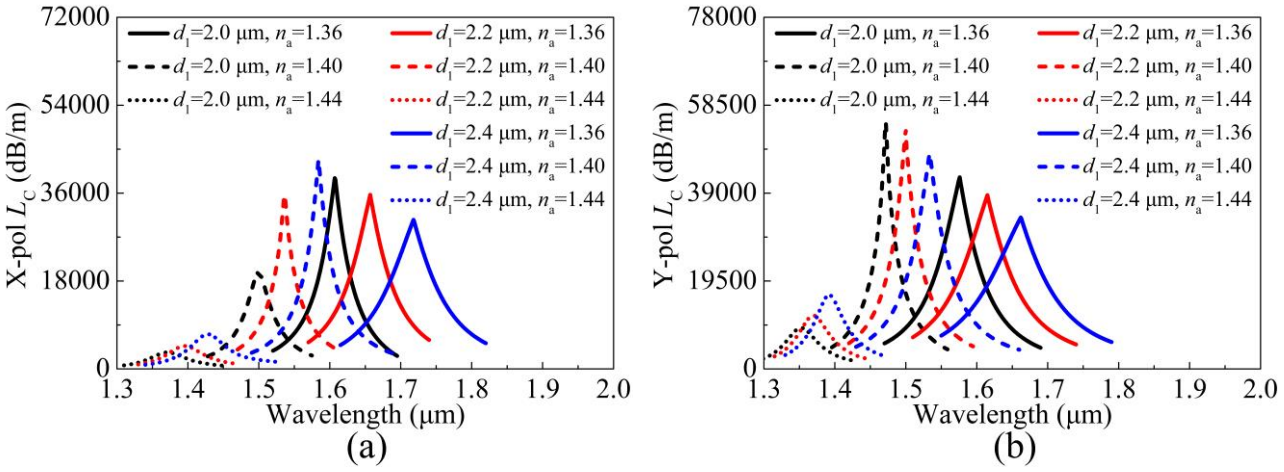

Fig. 5. The variation of the L_C of the **(a)** X-pol and **(b)** Y-pol core modes with wavelength for different d_1, when n_a is selected as 1.36, 1.40, and 1.44, respectively.

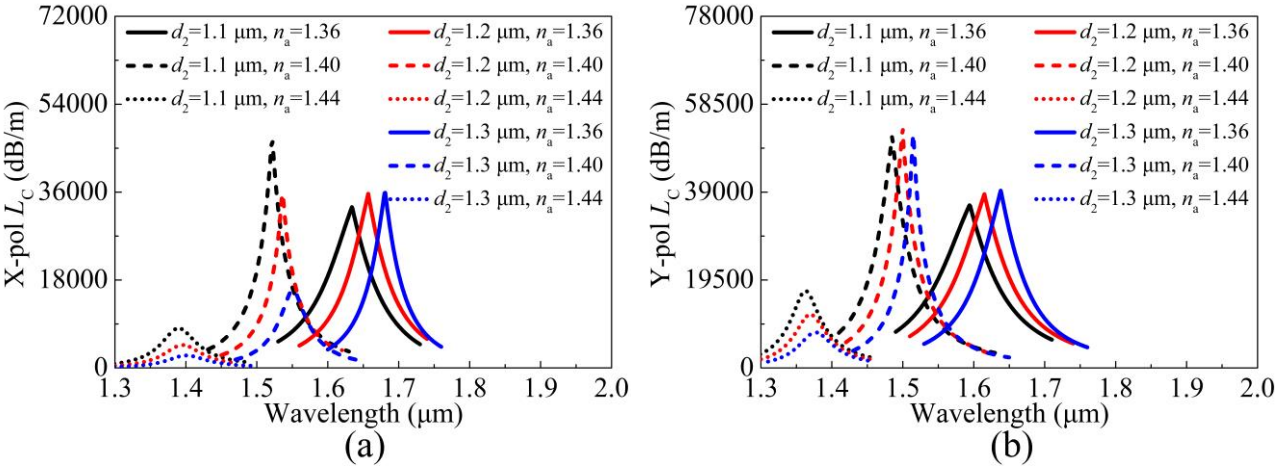

Fig. 6. The variation of the L_C of the **(a)** X-pol and **(b)** Y-pol core modes with wavelength for different d_2, when n_a is selected as 1.36, 1.40, and 1.44, respectively.

When n_a is selected as 1.36, 1.40, and 1.44, respectively, the variations of the L_C of the X-pol and Y-pol core modes with wavelength for different d_3 are shown in Fig. 7. From Figs. 7(a) and 7(b), when n_a is fixed at 1.36 1.40, or 1.44, the resonance wavelengths of the X-pol and Y-pol core modes have a significant red-shift with the increase of d_3 from 1.0 to 1.4 μm. At the same time, it is found that for different n_a, the resonant wavelength shifts of the X-pol and Y-pol core modes are basically the same with the increase of d_3. Different from the previous case, d_3 has a greater influence on the resonance wavelength for the complete and incomplete coupling cases. Therefore, with the change of d_3, the *WS* remains basically unchanged. That is to say, d_3 only affects the resonance wavelength shift, and has no influence on the *WS*.

When n_a is selected as 1.36, 1.40, and 1.44, respectively, the variations of the L_C of the X-pol and Y-pol core

modes with wavelength for different d_4 are shown in Fig. 8. From Figs. 8(a) and 8(b), when n_a is fixed at 1.36 or 1.40, the resonance wavelengths of the X-pol and Y-pol core modes have a significant blue-shift with the increase of d_4 from 1.5 to 1.7 μm. However, the resonance wavelengths of the X-pol and Y-pol core modes only have a weak blue-shift with the increase of d_4 from 1.5 to 1.7 μm, when n_a is fixed at 1.44. In other words, as n_a increases from 1.36 to 1.44, the blue-shift amplitude of the X-pol and Y-pol core modes decreases gradually with the increase of d_4. This also confirms that d_4 has a greater influence on the f resonance wavelength for the complete coupling case. Therefore, the smaller d_4, the greater the *WS*.

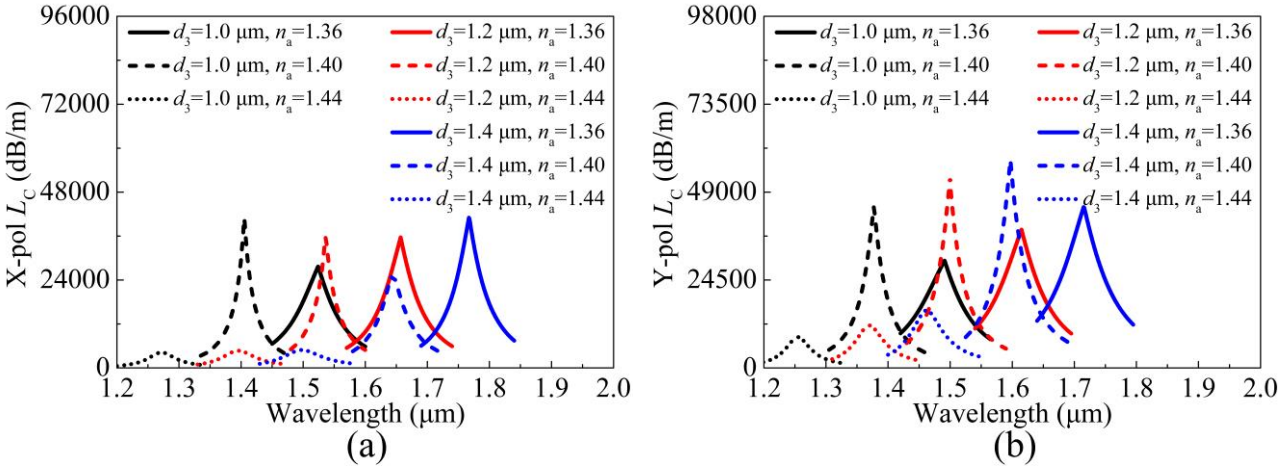

Fig. 7. The variation of the L_C of the **(a)** X-pol and **(b)** Y-pol core modes with wavelength for different d_3, when n_a is selected as 1.36, 1.40, and 1.44, respectively.

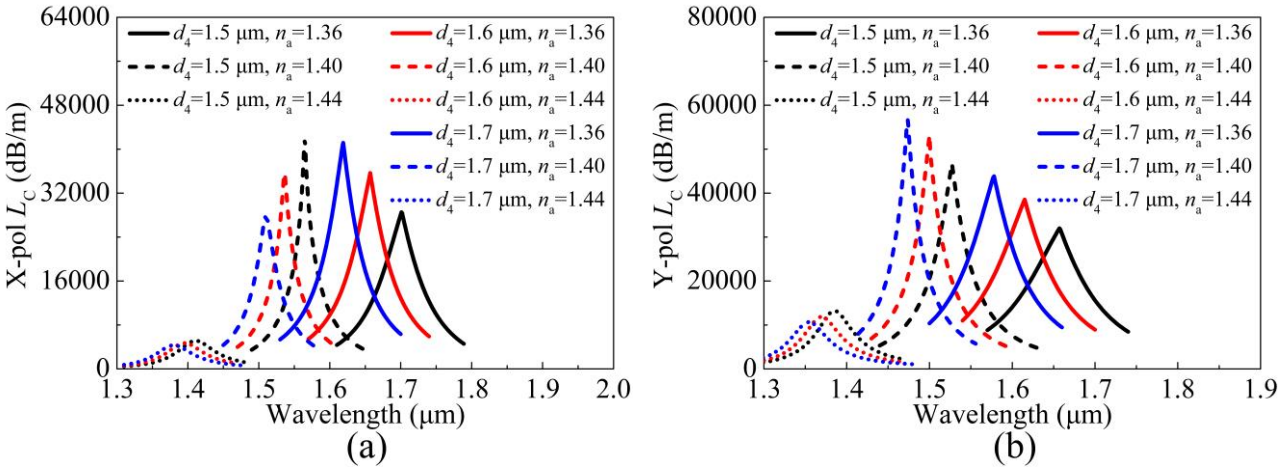

Fig. 8. The variation of the L_C of the **(a)** X-pol and **(b)** Y-pol core modes with wavelength for different d_4, when n_a is selected as 1.36, 1.40, and 1.44, respectively.

When n_a is selected as 1.36, 1.40, and 1.44, respectively, the variations of the L_C of the X-pol and Y-pol core modes with wavelength for different d_5 are shown in Fig. 9. From Figs. 9(a) and 9(b), when n_a is fixed at 1.36, the resonance wavelengths of the X-pol and Y-pol core modes only have a slight blue-shift with the increase of d_5 from 0.9 to 1.3 μm. Whether n_a is fixed at 1.40 or 1.44, the resonance wavelengths of the X-pol and Y-pol core modes have no obvious shift with the increase of d_5 from 0.9 to 1.3 μm. This also indicates that d_5 has a relatively greater influence on the resonance wavelength for the complete coupling case. However, the influence

of d_5 on the resonance wavelength is very small, so the influence of d_5 on the *WS* is negligible.

When n_a is selected as 1.36, 1.40, and 1.44, respectively, the variations of the L_C of the X-pol and Y-pol core modes with wavelength for different Λ are shown in Fig. 10. From Figs. 10(a) and 10(b), when n_a is fixed at 1.36 or 1.40, the resonance wavelengths of the X-pol and Y-pol core modes have a significant blue-shift with the increase of Λ from 2.1 to 2.5 μm. However, the resonance wavelengths of the X-pol and Y-pol core modes only have a small blue-shift with the increase of Λ from 2.1 to 2.5 μm when n_a is fixed at 1.44. That is to say, as n_a increases from 1.36 to 1.44, the blue-shift amplitude of the X-pol and Y-pol core modes decreases gradually with the increase of Λ. This is basically similar to the case of d_2. It also shows that Λ has a greater influence on the resonance wavelength for the complete coupling case. Thus, the smaller Λ, the greater the *WS*.

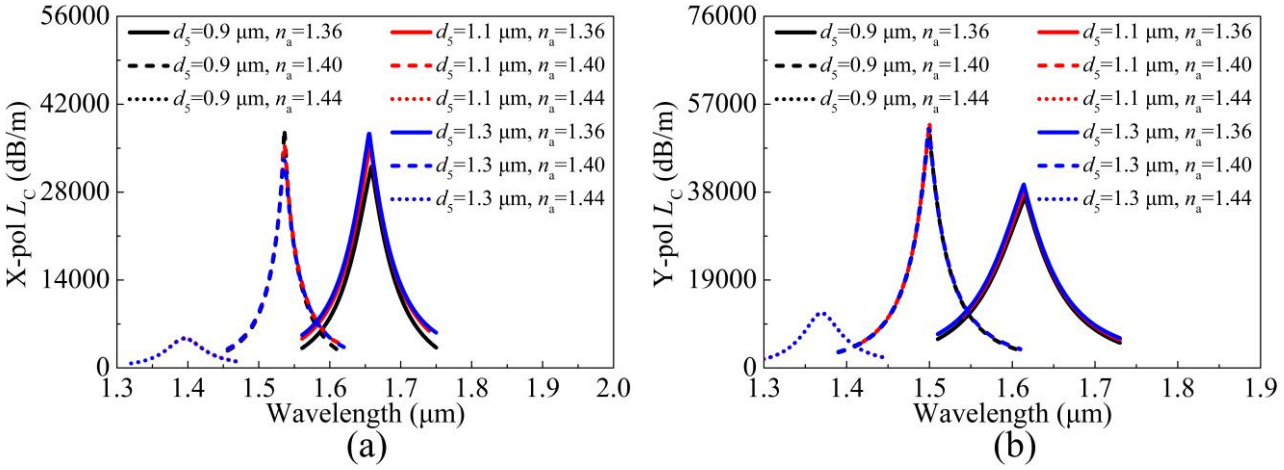

Fig. 9. The variation of the L_C of the **(a)** X-pol and **(b)** Y-pol core modes with wavelength for different d_5, when n_a is selected as 1.36, 1.40, and 1.44, respectively.

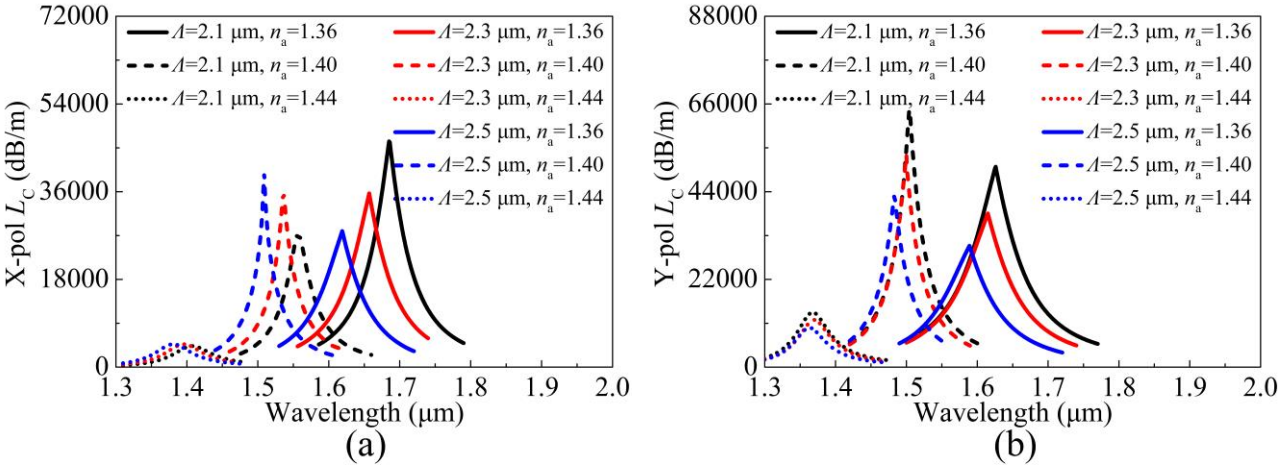

Fig. 10. The variation of the L_C of the **(a)** X-pol and **(b)** Y-pol core modes with wavelength for different Λ, when n_a is selected as 1.36, 1.40, and 1.44, respectively.

When n_a is selected as 1.36, 1.40, and 1.44, respectively, the variations of the L_C of the X-pol and Y-pol core modes with wavelength for different *t* are shown in Fig. 11. From Figs. 11(a) and 11(b), whether n_a is fixed at 1.36 1.40, or 1.44, as *t* increases from 45 to 55 nm, the resonance wavelengths of the X-pol and Y-pol core modes have a significant blue-shift. Similar to the case of d_3, *t* has a greater influence on the resonance wavelength for the

complete and incomplete coupling cases. Therefore, with the change of *t*, the *WS* basically does not change. In other words, *t* only affects the resonance wavelength, but has no influence on the *WS*. Finally, it is necessary to comprehensively consider the different effects of the above eight structure parameters on the resonance wavelength and *WS*, and then use the genetic algorithm for cyclic iterative optimization to obtain the final structure parameters [48, 49].

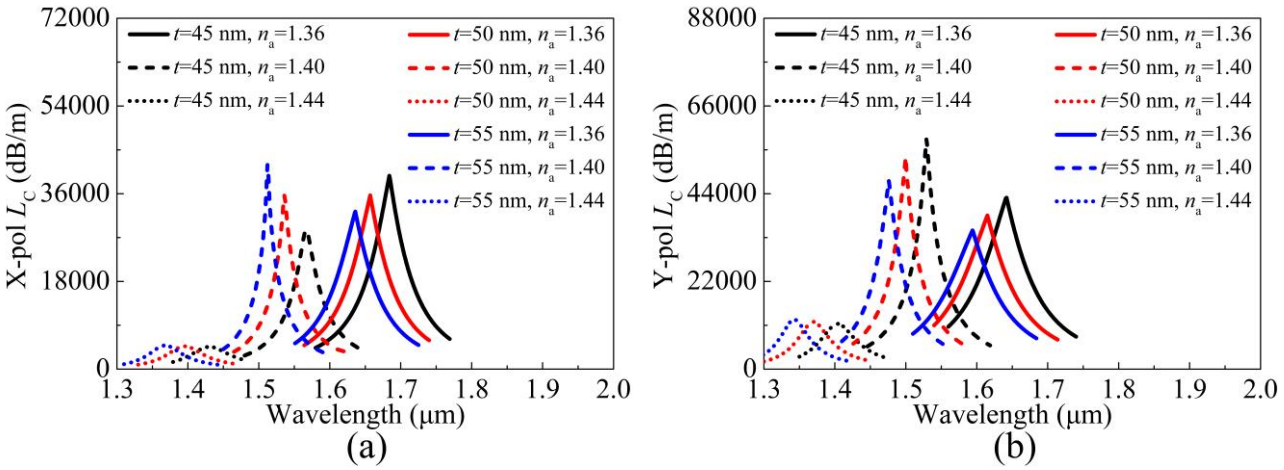

Fig. 11. The variation of the L_C of the **(a)** X-pol and **(b)** Y-pol core modes with wavelength for different *t*, when n_a is selected as 1.36, 1.40, and 1.44, respectively.

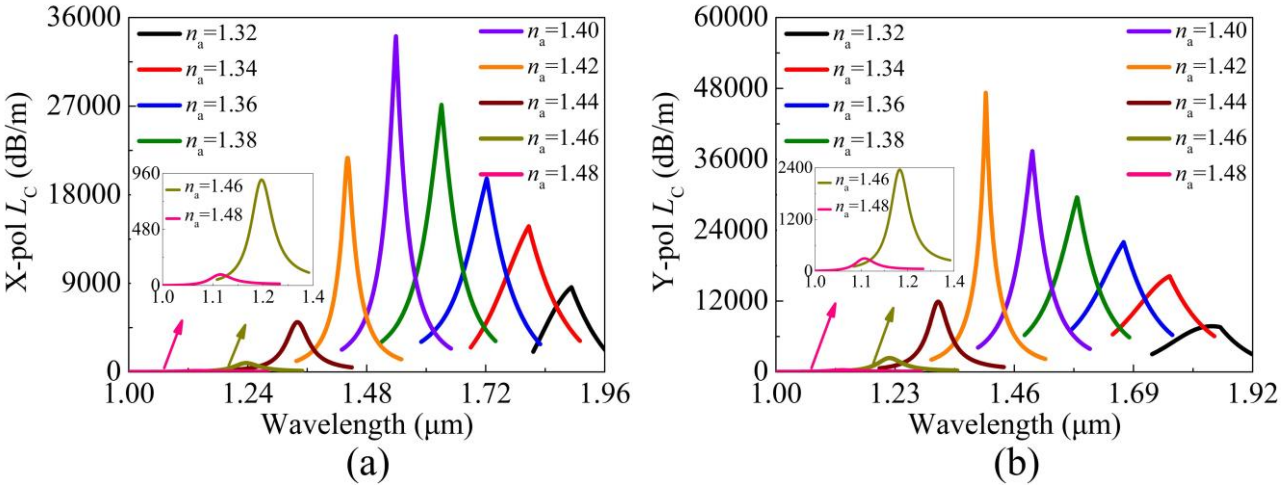

Fig. 12. The L_C of the **(a)** X-pol and **(b)** Y-pol core modes with wavelength when n_a is changed from 1.32 to 1.48. The illustrations in (a) and (b) show the local zoom-in results of the L_C of the X-pol and Y-pol core modes with wavelength when n_a is selected as 1.46 and 1.48, respectively.

By the genetic optimization iterative calculations, the final structure parameters are selected as follows: d_0=1.6 μm, d_1=2.35 μm, d_2=1.25 μm, d_3=1.1 μm, d_4=1.6 μm, d_5=1.22 μm, Λ=2.3 μm, and *t*=55 nm. When n_a is changed from 1.32 to 1.48, the L_C of the X-pol and Y-pol core modes are shown in Fig. 12. From Figs. 12(a) and 12(b), with the increase of n_a from 1.32 to 1.48, the resonance wavelengths of the X-pol and Y-pol core modes are gradually blue-shifted from 1.893 to 1.138 μm and 1.857 to 1.128 μm, respectively. When n_a is fixed at 1.40 and 1.42, respectively, the L_C of the X-pol and Y-pol core modes has the maximum resonance peaks at resonance wavelengths 1.539 μm and 1.405 μm, respectively. In addition, it can be seen from the illustrations in Figs. 12(a)

and 12(b) that there are still relatively large resonance peaks of the X-pol and Y-pol core modes when n_a is 1.46 and 1.48. When n_a is 1.48, the L_C of the X-pol and Y-pol core modes has the minimum resonance peaks at resonance wavelengths 1.138 μm and 1.128 μm, respectively. The difference between the maximum and minimum resonance peaks is very large. Therefore, the RI sensing can be realized when the analyte RI is changed from 1.32 to 1.48.

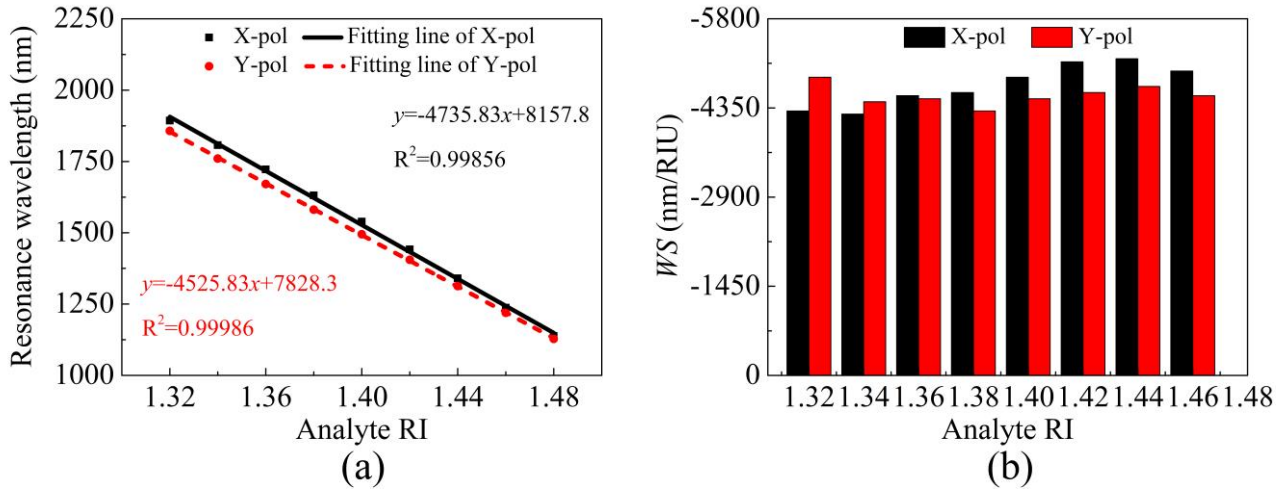

Fig. 13. (a) The linear fitting results of the resonance wavelengths for the X-pol and Y-pol core modes with the analyte RI and **(b)** the changes of the *WS* with the analyte RI, when the analyte RI is changed from 1.32 to 1.48.

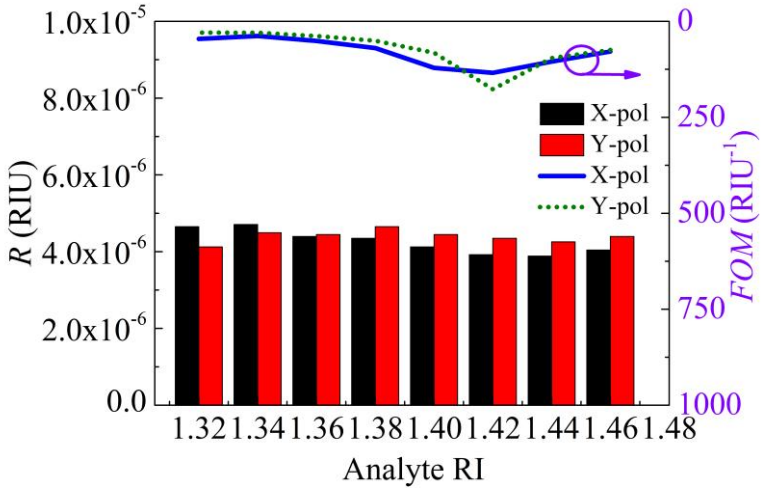

Fig. 14. The *R* and *FOM* with the analyte RI when the analyte RI is changed from 1.32 to 1.48.

Fig. 13(a) shows the linear fitting results of the resonance wavelengths for the X-pol and Y-pol core modes with the analyte RI. From Fig. 13(a), the linear fitting results of the X-pol and Y-pol core modes with the analyte RI are y= -4735.83x+8157.8 and y= -4525.83x+7828.3, respectively. And the R^2 of the X-pol and Y-pol core modes are 0.99856 and 0.99986, respectively, and the R^2 are greater than 0.998 for both the X-pol and Y-pol core modes. In the RI range of 1.32 to 1.48, the average *WSs* of the X-pol and Y-pol core modes can achieve -4735.83 nm/RIU and -4525.83 nm/RIU, respectively. Fig. 13(b) shows the changes of the *WS* with the analyte RI when the analyte RI is changed from 1.32 to 1.48. From Fig. 13(b), the maximum *WSs* of the X-pol and Y-pol core modes are -5150 nm/RIU and -4700 nm/RIU in the RI ranges of 1.44 to 1.46 and 1.44 to 1.46, respectively. The minimum *WSs* of the X-pol and Y-pol core modes are -4250 nm/RIU and -4300 nm/RIU in the RI ranges of 1.34

to 1.36 and 1.38 to 1.40, respectively. It can be concluded that the *WS* has a good linearity with the change of the analyte RI. Fig. 14 shows the changes of the *R* and *FOM* with the analyte RI when the analyte RI is changed from 1.32 to 1.48. From Fig. 14, the maximum *R* of the X-pol and Y-pol core modes are 4.71×10^{-6} RIU and 4.65×10^{-6} RIU in the RI ranges of 1.34 to 1.36 and 1.38 to 1.40, respectively. The maximum *FOM* of the X-pol and Y-pol core modes are 134 RIU^{-1} and 177 RIU^{-1} in the RI ranges of 1.40 to 1.42 and 1.40 to 1.42, respectively. In summary, the proposed SPR-PCF RI sensor simultaneously achieves the ultra wide detection range, high *WS*, good linearity, high *R*, and large *FOM*.

Table 2. Comparisons of the performance between the proposed SPR-PCF RI sensor and other reported SPR-PCF RI sensors.

Refs.	SPR-PCF RI sensor structures	RI range	*WS* (nm/RIU)	*R* (RIU)	*FOM* (RIU^{-1})
[33]	Coated with silver film on air hole and D-shape surface	1.33 ~ 1.38	3191.43	N/A	N/A
[34]	Coated with nano-ring gold film	1.40 ~ 1.43	2150	N/A	N/A
[35]	Coated with sliver and gold films on four analyte channels	X-pol 1.33 ~ 1.366 Y-pol 1.33 ~ 1.366	X-pol 1892 Y-pol 2337	X-pol 4×10^{-5} Y-pol 3.2×10^{-5}	N/A
[36]	Coated with gold film on one air hole	1.33 ~ 1.34	3500	N/A	39.8
[37]	Coated with gold film on D-shape surface	1.345 ~ 1.375	4494	N/A	N/A
This work	Coated with gold film on one air hole	X-pol 1.32 ~ 1.48 Y-pol 1.32 ~ 1.48	X-pol -4735.83 Y-pol -4525.83	X-pol 4.71×10^{-6} Y-pol 4.65×10^{-6}	X-pol 134 Y-pol 137

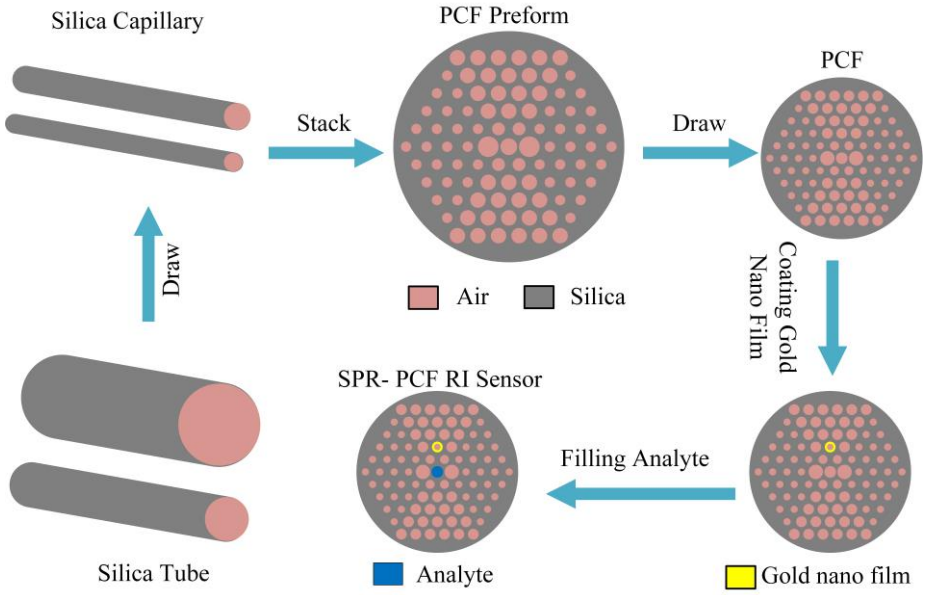

Fig. 15. The fabrication process of the proposed SPR-PCF RI sensor.

The comparisons of the performance between the proposed SPR-PCF RI sensor and other reported SPR-PCF RI sensors are shown in Table 2. From Table 2, compared with reported SPR-PCF RI sensors, the proposed SPR-PCF RI sensor has the widest analyte RI detection range of 1.32 to 1.48 and maximum average *WS*. In addition, it also has high *R* and large *FOM*. Moreover, it is worth noting that the structure of the proposed SPR-PCF RI sensor is relatively simple, which has great engineering advantages in the practical fabrication.

The fabrication process of the proposed SPR-PCF RI sensor is shown in Fig. 15. It can be seen from Fig. 15 that the fabrication process of the proposed SPR-PCF RI sensor can be divided into five steps. First, the high-purity silica tubes with different sizes are drawn into the silica capillaries with different sizes. Second, the high-purity silica capillaries with different sizes are stacked into the preform according to the designed cross-sectional structure of the PCF. Third, the PCF preform is drawn into the silica substrate PCF. Fourth, the gold nano film is coated on the air hole of the PCF by the chemical vapor deposition method. Fifth, with the capillary effect, the liquid analyte is filled into the central air hole of the PCF coated with the gold nano film. Finally, the proposed SPR-PCF RI sensor can be fabricated.

4. Conclusion

In summary, a novel SPR-PCF RI sensor coated with gold film is proposed. The different mode coupling effects of the X-pol and Y-pol core modes and 2nd-order SPP modes are analyzed when n_a is 1.36, 1.40, and 1.44, respectively. By considering the effects of the structure parameters on the resonance wavelength and *WS*, the final structure parameters are obtained. The average *WSs* of the X-pol and Y-pol core modes can achieve -4735.83 nm/RIU and -4525.83 nm/RIU, respectively, in the RI range of 1.32 to 1.48. In addition, the maximum *R* and *FOM* of the X-pol and Y-pol core modes are 4.71×10^{-6} RIU and 4.65×10^{-6} RIU, and 134 RIU^{-1} and 177 RIU^{-1}, respectively. Compared with the previous reported SPR-PCF RI sensors, the proposed SPR-PCF RI sensor has the advantages, including ultra wide detection range, high *WS*, good linearity, high *R*, and large *FOM*, so it can find important applications in the fields of biochemistry, medicine, and environmental science.

Acknowledgements

This work was supported in part by the National Natural Science Foundation of China (Granted No. 61875238).

Declaration of competing interest

The authors declare that they have no known competing financial interests or personal relationships that could have appeared to influence the work reported in this paper.

CRediT authorship contribution statement

Yuwei Qu: Conceptualization, Formal analysis, Writing-original draft, Methodology, Investigation. **Jinhui Yuan**: Supervision, Formal analysis, Methodology, Writing-review & editing. **Shi Qiu**: Supervision, Formal analysis, Writing-review & editing. **Xian Zhou**: Supervision, Formal analysis, Writing-review & editing. **Binbin Yan**: Formal analysis, Writing-review & editing. **Qiang Wu**: Supervision, Formal analysis, Methodology, Writing-review & editing. **Bin Liu**: Formal analysis, Writing-review & editing. **Kuiru Wang**: Formal analysis, Writing-review & editing. **Xinzhu Sang**: Supervision, Writing-review & editing. **Keping Long**: Supervision, Writing-review & editing. **Chongxiu Yu**: Supervision, Writing-review & editing.

References

[1] J. C. Knight, T. A. Birks, P. St. J. Russell, D. M. Atkin, All-silica single-mode optical fiber with photonic crystal cladding, Opt.

Lett. 21 (1996) 1547-1549.

[2] Y. N. Zhu, Z. H. He, H. Du, Detection of external refractive index change with high sensitivity using long-period gratings in photonic crystal fiber, Sens. Actuators B Chem. 131 (2008) 265-269.

[3] R. Jha, J. Villatoro, G. Badenes, Ultrastable in reflection photonic crystal fiber modal interferometer for accurate refractive index sensing, Appl. Phys. Lett. 93 (2008) 191106.

[4] Y.L. Hoo, W. Jin, L. Xiao, J. Ju, H.L. Ho, Numerical study of refractive index sensing based on the anti-guide property of a depressed-index core photonic crystal fiber, Sens. Actuators B Chem. 136 (2009) 26-31.

[5] G. E. Town, W. Yuan, R. McCosker, O. Bang, Microstructured optical fiber refractive index sensor, Opt. Lett. 35 (2010) 856-858.

[6] Y. Zhao, Z. Q. Deng, J. Li, Photonic crystal fiber based surface plasmon resonance chemical sensors, Sens. Actuators B Chem. 202 (2014) 557-567.

[7] M. Tian, P. Lu, L. Chen, C. Lv, D. M. Liu, All-solid D-shaped photonic fiber sensor based on surface plasmon resonance, Opt. Commun. 285 (2012) 1550-1554.

[8] H. L. Chen, S. G. Li, J. S. Li, Z. K. Fan, Magnetic field sensor based on magnetic fluid selectively infilling photonic crystal fibers, IEEE Photon. Technol. Lett. 27 (2015) 717-720.

[9] M. F. O. Hameed, M. Y. Azab, A. M. Heikal, S. M. El-Hefnawy, S. S. A. Obayya, Highly sensitive plasmonic photonic crystal temperature sensor filled with liquid crystal, IEEE Photon. Technol. Lett. 28 (2016) 59-62.

[10] Q. Liu, P. S. Xue, Z. Y. Liu, Voltage sensor based on liquid-crystal-infiltrated photonic crystal fiber with high index, Appl. Phys. Express 13 (2020) 032005.

[11] Q. Liu, Z. Ma, Q. Wu, W. L. Wang, The biochemical sensor based on liquid-core photonic crystal fiber filled with gold, silver and aluminum, Opt. Laser Technol. 130 (2020) 106363.

[12] J. Wang, L. Pei, J. S. Wang, Z. L. Ruan, J. J. Zheng, J. Li, T. G. Ning, Magnetic field and temperature dual-parameter sensor based on magnetic fluid materials filled photonic crystal fiber, Opt. Express 28 (2020) 1456-1471.

[13] H. Chen, Z. H. Chen, H. Yang, L. H. Wen, Z. Yi, Z. G. Zhou, B. Dai, J. G. Zhang, X. W. Wu, P. H. Wu, Multi-mode surface plasmon resonance absorber based on dart-type single-layer graphene, Res Adv. 12 (2022) 7821-7829.

[14] F. Zhao, J. C. Lin, Z. H. Lei, Z. Yi, F. Qin, J. G. Zhang, L. Liu, X. W. Wu, W. X. Yang, P. H. Wu, Realization of 18.97% theoretical efficiency of 0.9 μm thick C-Si/ZnO heterojunction ultrathin-film solar cells via surface plasmon resonance enhancement, Phys. Chem. Chem. Phys. 24 (2022) 4871-4880.

[15] Z. P. Zheng, Y. Zheng, Y. Luo, Z. Yi, J. G. Zhang, Z. M. Liu, W. X. Yang, Y. Yu, X. W. Wu, P. H. Wu, A switchable terahertz device combining ultra-wideband absorption and ultra-wideband complete reflection, Phys. Chem. Chem. Phys. 24 (2022) 2527-2533.

[16] Z. P. Zheng, Y. Luo, H. Yang, Z. Yi, J. G. Zhang, Q. J. Song, W. X. Yang, C. Liu, X. W. Wu, P. H. Wu, Thermal tuning of terahertz metamaterial absorber properties based on VO_2, Phys. Chem. Chem. Phys. 24 (2022) 8846-8853.

[17] F. Q. Zhou, F. Qin, Z. Yi, W. T. Yao, Z. M. Liu, X. W. Wu, P. H. Wu, Ultra-wideband and wide-angle perfect solar energy absorber based on Ti nanorings surface plasmon resonance, Phys. Chem. Chem. Phys. 213 (2021) 17041-17048.

[18] X. Yan, R. Fu, T. L. Cheng, S. G. Li, A highly sensitive refractive index sensor based on a V-Shaped photonic crystal fiber with a high refractive index range, Sensors 21 (2021) 3782.

[19] Y. J. Wang, S. G. Li, J. S. Li, Y. Guo, M. Y. Wang, Novel external gold-coated side-leakage photonic crystal fiber for tunable broadband polarization filter, J. Lightw. Technol. 39 (2021) 1791-1799.

[20] L. Wu, H. S. Chu, W. S. Koh, E. P. Li, Highly sensitive graphene biosensors based on surface plasmon resonance, Opt. Express 18 (2010) 14395-14400.

[21] S. H. Choi, Y. L. Kim, K. M. Byun, Graphene-on-silver substrates for sensitive surface plasmon resonance imaging biosensors, Opt. Express 19 (2011) 458-466.

[22] M. Piliarik, H. Šípová, P. Kvasnička, N. Galler, J. R. Krenn, J. Homola, High-resolution biosensor based on localized surface plasmons, Opt. Express 20 (2011) 672-680.

[23] U. Bog, K. Huska, F. Maerkle, A. Nesterov-Mueller, U. Lemmer, T. Mappes, Design of plasmonic grating structures towards optimum signal discrimination for biosensing applications, Opt. Express 20 (2012) 11357-11369.

[24] H. Y. Lin, C. H. Huang, G. L. Cheng, N. K. Chen, H. C. Chui, Tapered optical fiber sensor based on localized surface plasmon resonance, Opt. Express 20 (2012) 21693-21701.

[25] A. A. Rifat, R. Ahmed, A. K. Yetisen, H. Butt, A. Sabouri, G. A. Mahdiraji, S. H. Yun, F. R. M. Adikan, Photonic crystal fiber based plasmonic sensors, Sens. Actuators B Chem. 243 (2017) 311-325.

[26] Q. Liu, J. D. Sun, Y. D. Sun, Z. H. Ren, C. Liu, J. W. Lv, F. M. Wang, L. Y. Wang, W. Liu, T. Sun, P. K. Chu, Surface plasmon resonance sensor based on photonic crystal fiber with indium tin oxide film, Opt. Mater. 102 (2020) 109800.

[27] U. Ramani, H. Kumar, B. K. Singh, P. C. Pandey, Study of highly sensitivity metal wires assisted photonic crystal fber based refractive index sensor, Opt. Quant. Electron. 52 (2020) 521.

[28] Z. X. Tan, X. J. Li, Y. Z. Chen, P. Fan, Improving the sensitivity of fiber surface plasmon resonance sensor by filling liquid in a hollow core photonic crystal fiber, Plasmonics 9 (2013) 1-7.

[29] N. N. Luan, R. Wang, W. H. Lv, J. Q. Yao, Surface plasmon resonance sensor based on D-shaped microstructured optical fiber with hollow core, Opt. Express 23 (2015) 8576-8582.

[30] G. W. An, S. G. Li, W. Qin, W. Zhang, Z. K. Fan, Y. J. Bao, High-sensitivity refractive index sensor based on D-shaped photonic crystal fiber with rectangular lattice and nanoscale gold film, Plasmonics 9 (2014) 1355-1360.

[31] C. Liu, L. Yang, X. L. Lu, Q. Liu, F. M. Wang, J. W. Lv, T. Sun, H. W. Mu, P. K. Chu, Mid-infrared surface plasmon resonance sensor based on photonic crystal fibers, Opt. Express 25 (2017) 14227-14237.

[32] A. A. Rifat, F. Haider, R. Ahmed, G. A. Mahdiraji, F. R. M. Adikan, A. E. Miroshnichenko, Highly sensitive selectively coated photonic crystal fiber-based plasmonic sensor, Opt. Lett. 43 (2018) 891-894.

[33] C. Zhou, H. K. Zhang, P. Song, J. Wang , C. G. Zhu, P. P. Wang, F. Peng, D-shaped photonic crystal fiber plasmon sensors based on self-reference channel, IEEE Photon. Technol. Lett. 32 (2020) 589-591.

[34] Z. K. Fan, Surface plasmon resonance refractive index sensor based on photonic crystal fiber covering nano-ring gold film, Opt. Fiber Technol. 50 (2019) 194-199.

[35] A. Yasli, H. Ademgil, S. Haxha, A. Aggoun, Multi-channel photonic crystal fiber based surface plasmon resonance sensor for multi-analyte sensing, IEEE Photo. J. 12 (2020) 6800515.

[36] S. Wang, X. H. Sun, Y. H. Luo, G. D. Peng, Surface plasmon resonance sensor based on D-shaped Hi-Bi photonic crystal fiber, Opt. Commun. 467 (2020) 125675.

[37] J. J. Wu, C. Dou, L. C. Hu, The D-shape elliptical stoma photonic crystal fiber based on surface plasmon resonance with both filtering and sensing, Opt. Quant. Electron. 53 (2021) 565.

[38] G. Y. Wang, Y. Lu, X. C. Yang, L. C. Duanm J. Q. Yao, High-sensitivity magnetic field sensor based on a dual-core photonic crystal fiber, Appl. Opt. 58 (2019) 5800-5806.

[39] F. M. Wang, C. Liu, Z. J. Sun, T. Sun, B. H. Liu, P. K. Chu, A highly sensitive SPR sensors based on two parallel PCFs for low refractive index detection, IEEE Photo. J. 10 (2018) 7104010.

[40] J. S. Wang, L. Pei, J. Wang, Z. L. Ruan, J. J. Zheng, J. Li, Surface plasmon resonance sensor for low refractive index detection based on microstructured fiber, J. Opt. Soc. Am. B 36 (2019) 3104-3110.

[41] X. Yan, R. X. Shen, T. L. Cheng, S. G. Li, Research on filtering characteristics of asymmetric photonic crystal fiber based on gold coating, Opt. Commun. 488 (2021) 126860.

[42] C. Liu, J. W. Wang, F. M. Wang, W. Q. Su, L. Yang, J. W. Lv, G. L. Fu, X. L. Li, Q. Liu, T. Sun, P. K. Chu, Surface plasmon resonance (SPR) infrared sensor based on D-shape photonic crystal fibers with ITO coatings, Opt. Commun. 464 (2020) 125496.

[43] J. S. Wang, L. Pei, L. Y. Wu, J. Wang, Z. L. Ruan, J. J. Zheng, A polarization-independent SPR sensor based on photonic crystal fiber for low RI detection, Plasmonics 15 (2020) 327-333.

[44] Q. Liu, J. D. Sun, Y. D. Sun, W. Liu, F. M. Wang, L. Yang, C. Liu, Q. Y. Liu, Q. Li, Z. H. Reng, T. Sun, P. K. Chu, Surface plasmon resonance sensor based on eccentric core photonic quasi-crystal fiber with indium tin oxide, Appl. Opt. 58 (2019)

6848-6853.

[45] Y. C. Liu, S. G. Li, H. L. Chen, J. S. Li, W. X. Zhang, M. Y. Wang, Surface plasmon resonance induced high sensitivity temperature and refractive index sensor based on evanescent field enhanced photonic crystal fiber, J. Lightw. Technol. 38 (2019) 919-928.

[46] A.W. Snyder, J. D. Love, Optical Waveguide Theory, Chapman&Hall: London, the United Kingdom (1983) 542-552.

[47] Z. H. Zhang, Y. F. Shi, B. M. Bian, J. Lu, Dependence of leaky mode coupling on loss in photonic crystal fiber with hybrid cladding, Opt. Express 16 (2008) 1915-1922.

[48] I. Abdelaziz, F. AbdelMalek, S. Haxha, H. Ademgil, H. Bouchriha, Photonic crystal fiber with an ultrahigh birefringence and flattened dispersion by using genetic algorithms, J. Lightw. Technol. 31 (2013) 343-348.

[49] L. L. Zhang, Y. C. Meng, Design and analysis of a photonic crystal fiber supporting stable transmission of 30 OAM modes, Opt. Fiber Technol. 61 (2021) 102423.